Synthesis of ZnO/Bi-doped porous LaFeO$_3$ nanocomposites as highly efficient nano-photocatalysts dependent on the enhanced utilization of visible-light-excited electrons

Muhammad Humayun, Ning Sun, Fazal Raziq, Xuliang Zhang, Rui Yan, Zhijun Li, Yang Qu*, Liqiang Jing*

Key Laboratory of Functional Inorganic Materials Chemistry (Heilongjiang University), Ministry of Education, School of Chemistry and Materials Science, International Joint Research Center for Catalytic Technology, Harbin 150080, China

ARTICLE INFO

ABSTRACT

ZnO coupled Bi-doped porous LaFeO$_3$ nanocomposites have successfully been fabricated via a wet-chemical method. It is confirmed that Bi^{3+} enters into the crystal lattice of PLFO and substitute La^{3+}, while the ZnO with diameter of ~15 nm is coupled to the Bi-doped PLFO. It is shown that the amount-optimized 5Zn/7Bi-PLFO nanocomposite exhibits greatly improved visible-light activities for 2,4-dichlorophenol (2,4-DCP) degradation and CO$_2$ conversion, compared to the unmodified PLFO with rather high photoactivity due to its large specific surface area. Based on the measurements of valence band XPS spectra, steady-state surface photovoltage spectra, transient-state surface photovoltage responses, photoelectrochemical I–V curves, fluorescence spectra related to produced ·OH amount and photocurrent action spectra, it is clearly demonstrated that the significantly improved visible-light activities are attributed to the enhanced utilization of visible-light-excited high-level-energy electrons (HLEEs) by coupling with nanocrystalline ZnO to introduce a new energy platform for accepting electrons and to the extended visible-light absorption by doping Bi^{3+} to create surface states. Interestingly, it is proved that under UV–vis irradiation, the amount-optimized nanocomposite exhibit much higher photoactivity for 2,4-DCP degradation compared to the commercially available P25 TiO$_2$. Moreover, it is confirmed by means of radical trapping experiments that the dominant radicals to decompose 2,4-DCP on PLFO could be modulated by doping Bi^{3+} and coupling ZnO. Furthermore, the possible decomposition pathways, respectively related to the ·OH and O$_2$·$^-$, of 2,4-DCP over the amount-optimized Bi-doped PLFO and ZnO coupled Bi-doped PLFO samples are proposed by means of the liquid chromatography tandem mass spectrometry analysis of the intermediates, especially with the used isotopic D$_2$O.

1. Introduction

The environmental deterioration problems, especially water contamination have interrupted the balance of harmonious coexistence between nature and human beings in recent few years [1]. The release of hazardous inorganic and organic by-products in the industrial wastewater and domestic sewage has been far beyond the natural degradation capability of the ecosystem [2]. Particularly, the chlorophenols as the most hazardous organic pollutants are widely used in the production of pesticides, bactericides and wood preservatives. Due to the high stability of chlorine-carbon bonds, chlorophenols are difficult to biodegrade and have been listed by the US EPA as priority control pollutants [3]. Generally, the most hazardous 2,4-dichlorophenol (2,4-DCP) has been included in the Drinking Water

Contaminant Candidate List (CCL). It is a long-lived pollutant and its use has been strictly restrained because of its carcinogenic properties [4,5]. Several physicochemical, thermal and conventional biological methods including activated carbon adsorption, incineration and biological degradation have been widely explored to remove 2,4-DCP from the contaminated water. However, these techniques always exhibit shortfalls, such as physicochemical techniques usually require a post treatment for the removal of pollutant from the newly contaminated environment, thermal treatments always give rise to secondary hazardous pollutants, while biological methods require a long time treatment for the degradation of pollutants by microorganisms because they are affected by the chlorophenols toxicity [6].

On the other hand, the vast quantity of CO$_2$ accumulating in the atmosphere as a result of energy consumption, primarily via the

combustion of fossil fuels, vehicle exhaust and industrial activities has a devastating impact on the global climate [7]. With the current increase in rate of atmospheric CO_2 concentration, it is estimated that the average global temperature will increase by 6 °C at the end of 21st century, which will swing earth's climate from glacial to an ice-free Antarctica [8]. Therefore, it is highly desirable to convert CO_2 into useful fuels for sustainable energy production. In this regard, several electrocatalytic and traditionally biological methods have been widely investigated [9]. However, these techniques are always involved with poor stability, electrode corrosion, low mechanical strength and catalytic poisoning [10]. Therefore, it is of great significance to develop environmental friendly and alternative techniques to overcome the above-mentioned drawbacks.

As a promising alternative technique, semiconductor photocatalysis has received much attention in the past decade owing to its low cost, high stability, non-toxicity and environmental friendly merits. TiO_2 is the mostly investigated semiconductor photocatalyst in this regard [11–19]. However, it exhibits photocatalytic activity only under UV irradiation. Since the visible-light accounts for ca. 46% of the solar spectrum, it is highly desirable to develop visible-light responsive narrow bandgap photocatalysts for effective solar energy utilization [20]. In past few years, narrow bandgap photocatalysts such as Ag_3PO_4, $BiFeO_3$, WO_3 and $BiVO_4$ have been widely studied for effective degradation of chlorophenols and CO_2 conversion [21–26]. However, the weak photocatalytic performance and ambiguous photocatalytic mechanisms still greatly limits their use as efficient photocatalysts. Recently, perovskite-type ABO_3 oxides have attracted much attention in the field of photocatalysis due to their special structure. These oxides exhibit superior photocatalytic activity because of the corner-shared BO_6 octahedron which facilitates electron transfer [27]. In particular, the visible-light active $LaFeO_3$ (LFO) is of great interest due to its low cost, high stability, non-toxicity and suitable band gap ~ 2.0 eV [28]. It has been extensively utilized in the field of electrocatalysis and photocatalysis. However, it still exhibits weak photocatalytic activity, which is attributed to the low utilization of visible-light excited high-level energy electrons (HLEEs) and limited visible-light absorption [29].

Although the CB bottom of PLFO is located at 0.2 eV vs. NHE, the visible-light excited HLEEs above 0 eV should possess strong capacity to induce reduction reactions. However, these HLEEs would quickly relax to the bottom of CB so as to greatly lose its potential energy. Hence, it is of great significance to develop a reasonable strategy to utilize the visible-light excited HLEEs of PLFO for efficient photocatalysis. Interestingly, it has been preliminarily demonstrated in our previous reports [30–32], that the visible-light excited HLEEs of narrow bandgap semiconductors such as Fe_2O_3, $BiVO_4$ and $BiFeO_3$ could transfer thermodynamically to the conduction band of TiO_2 with a high-energy level platform, leading to the prolonged lifetime of photogenerated charge carriers and hence to the improved visible-light activities. Similar to TiO_2, ZnO is also a typical wide-bandgap semiconductor. However, its CB bottom (−0.1 eV) is less negative than that of TiO_2 (−0.3 eV) [33]. Accordingly, it is much feasible to utilize the photogenerated HLEEs of PLFO in photocatalysis by coupling with ZnO to introduce a more suitable high-energy level platform. Unfortunately, related works to LFO have not been reported up to date.

In addition, the visible-light-response of LFO could be extended by introducing foreign atoms into its crystal lattice [34,35]. According to the valence band position (2.2 eV) of LFO, it is expected that the photogenerated holes should possess sufficient energy to induce oxidation reactions with H_2O or directly oxidize organic pollutants. Hence, it is vital to decrease the intrinsic bandgap of PLFO by doping metal and non-metal elements. The dopants introduced surface states would shift its valence band top upward to a certain degree [3]. Thus, the photocatalytic activities of PLFO could be greatly enhanced by the visible-light extension. Unfortunately, related works to perovskite-type PLFO have seldom been reported to date. Generally, it is accepted that

bismuth based oxides have reduced bandgaps with strong visible-light absorption capacity, high stability and facile hole mobility due to the filled Bi 6s orbital of Bi^{+3} and empty 6s orbital of Bi^{+5}. When Bi is introduced in the crystal lattice of narrow bandgap oxides, the Bi 6s and O 2p orbitals in the valence band form a pair of occupied bonding and anti-bonding states, consequently leading to the reduced bandgap [36]. Therefore, it is a feasible approach to extend the visible-light absorption of PLFO by doping Bi for high visible-light photoactivity.

Generally, for semiconductor photocatalysis, it is of great significance to deeply explore the roles of photogenerated e^-/h^+ pairs and the induced highly-active species like OH and $O_2^{\cdot-}$ radicals in the photocatalytic process, which have been regarded as the critical intermediates to subsequently initiate redox reactions. The formed OH radicals have been considered as the primary oxidants with no selectivity to organic pollutants, while the produced $O_2^{\cdot-}$ ones are also vital active species that could oxidize a wide range of organic contaminants such as pesticides, dioxins and chlorinated solvents. The $O_2^{\cdot-}$ species generated in solution are strongly nucleophilic and directly attack the carbon atoms to cleave the bonds between the chlorine and carbon atoms [37–39]. Although several works have been reported on the determination of highly active species by means of electronic spin resonance and transient spectroscopic methods [40,41], but the photocatalytic mechanisms are still not fully understood, even ambiguous. This is mainly because that the photocatalytic mechanisms are strongly influenced by different photocatalysts and model pollutants. In addition, it is expected that different dominant radical species would decide the final photoactivity and the decomposition paths. In other words, the modulation of dominant radical species is possibly beneficial to improve the photocatalytic activity. Therefore, it is meaningful to explore the dominant radical species and their modulation for efficient photocatalysis to decompose 2,4-DCP.

Herein, we report the synthesis of ZnO coupled Bi-doped PLFO as efficient visible-light photocatalysts for 2,4-DCP degradation and CO_2 conversion. It is demonstrated that the significantly improved visible-light activities of PLFO are attributed to the enhanced utilization of visible-light-excited HLEEs by coupling with ZnO to introduce a new energy platform for accepting electrons and to the extended visible-light absorption by doping Bi^{3+} to create surface states. It is noteworthy that under UV–vis irradiation, the amount-optimized 5Zn/7Bi-PLFO sample could exhibit much higher photoactivity for 2,4-DCP degradation as compared to the P25 TiO_2. Moreover, it is confirmed that the dominant radicals to decompose 2,4-DCP on PLFO could be modulated by doping Bi^{3+} and coupling ZnO from OH to $O_2^{\cdot-}$. Furthermore, the possible decomposition pathways, respectively related to the OH and $O_2^{\cdot-}$, of 2,4-DCP over the amount-optimized 7Bi-PLFO and 5Zn/7Bi-PLFO samples are proposed by means of isotopic D_2O experiments. This work opens up a new feasible strategy for the synthesis of highly-efficient visible-light-active perovskite-type nanophotocatalysts for environmental remediation and energy production.

2. Experimental section

2.1. Material synthesis

All the reagents were of analytical grade and used without further purification. De-ionized water was used throughout the experiments. Amino-functionalized carbon (AC) nanospheres as templates were prepared according to our previous report [3]. Porous LFO (PLFO) nanoparticles were synthesized by a sol-gel method. In a typical procedure, stoichiometric amounts (0.04 mol) of $La(NO_3)_3 \cdot 6H_2O$ and $Fe(NO_3)_3 \cdot 9H_2O$ were dissolved into a mixed solvent of ethylene glycol (EG), ethanol and deionized water in 1:1:2 at room temperature. After that, AC nanospheres (0.2 g) were dispersed into the precursor solution by ultrasonic treatment for 30 min. Then the mixture was kept under stirring for 4 h. Finally, the mixture was dried in oven at 80 °C and calcined in air at 400 °C (temp ramp 1 °C min^{-1}) for 2 h to remove AC

template, and then annealed at 600 °C (5 °C min^{-1}) for 2 h to obtain PLFO nanoparticles.

To prepare different mole ratio percentage of Bi-doped PLFO samples, certain amounts of Bi(NO$_3$)$_3$·5H$_2$O were added into the PLFO precursor solution, prepared in a 1:1:2 mixture of ethylene glycol (EG), ethanol and deionized water. Then 0.2 g of AC nanospheres was dispersed into the above precursor solution by ultrasonication for 30 min. The mixture was continuously stirred for 4 h and then dried in oven at 80 °C. Finally, the product was calcined in air at 400 °C (temp ramp 1 °C min^{-1}) for 2 h to remove AC template, and then annealed at 600 °C (5 °C min^{-1}) for 2 h to obtain XBi-PLFO samples, in which X is the mole ratio percentage (1, 5, 7, 10%) of Bi to PLFO.

To prepare different mass ratio percentage ZnO coupled PLFO and Bi-doped PLFO nanocomposites, for each sample 1 g freshly prepared PLFO and 7Bi-PLFO samples was taken and dispersed into a mixed solvent (50–50 vol %) of ethanol and deionized water. Then different mass ratio percentage (1, 5, 7 and 10%) of the as-prepared ZnO was added to each mixture. The mixtures were vigorously stirred for 6 h and then dried in oven at 80 °C. Finally, the mixtures were annealed at 450 °C for 2 h to obtain the nanocomposites. The nanocomposites were represented by YZn-PLFO and YZn/7Bi-PLFO, where Y is the mass ratio percentage of ZnO to PLFO and 7Bi-PLFO samples.

2.2. Characterization

The X-ray diffraction patterns of the materials were performed using Bruker D8 powder diffractometer (Japan), with Cu$_{K\alpha}$ radiation (α = 0.15418 nm). The UV–vis diffuse reflectance spectra (UV–vis DRS) were obtained with Shimadzu UV-2550 Spectrophotometer (Japan). The transmission electron microscopy (TEM) images were taken with a model (JEM-2100, JEOL, Japan) operated at 200 kV. The N$_2$ adsorption–desorption isotherms were recorded with Micromeritics Tristar II 3020 system (U.S.A). The surface composition and elemental chemical states of the samples were examined by X-ray photoelectron spectroscopy (XPS) using a Kratos-Axis Ultra DLD apparatus (Japan) with an Al (mono) X-ray source and the binding energies of the samples were calibrated with respect to the signal for adventitious carbon (C1s) at 284.6 eV. The element composition of the samples was measured with the help of energy dispersive X-ray (EDX), using JEM-2100 electron microscope (JEOL, Japan) equipped with an EDS probe.

The steady-state surface photovoltage spectra (SS-SPS) were recorded with a home-built apparatus, equipped with a lock-in amplifier (SR830, USA) synchronized with a light chopper (SR540, USA). Time-resolved surface photovoltage (TR-SPV) responses were taken by connecting the sample chamber to an ITO glass at the electrode top and a steel substrate at the electrode bottom, and to decrease the space charge region at the ITO-sample interface, a 10 μm thick mica spacer was placed between ITO glass and the sample. The TR-SPV measurements were performed in air atmosphere at room temperature. The samples were excited by a 532 nm irradiation pulse, with 10 ns width from the second harmonic of a neodymium-doped yttrium aluminum garnet (Nd: YAG) laser (Lab-130-10H, Newport, Co.). Intensity of the pulse was recorded by a high-energy pyroelectric sensor (PE50BF-DIF-C, Ophir Photonics Group). The TR-SPV signals were amplified with a pre-amplifier and registered with a 1 GHz digital phosphor oscilloscope (DPO 4104B, Tektronix).

2.3. Photoelectrochemical measurements

For photoelectrochemical (PEC) measurement, the electrode films were prepared by the following procedure: for each film, 0.05 g of the powder sample was dispersed in 2 mL of isopropyl alcohol under ultrasonic treatment for 0.5 h. Then, the mixtures were kept under stirring for 0.5 h. To each mixture, 0.025 g of Macrogol-6000 was added and kept under ultrasonic treatment for another 0.5 h. Finally, 0.1 mL of acetylacetone was added to each mixture and kept under magnetic

stirring for 72 h. For the paste synthesis, the conductive fluorine-doped tin oxide (FTO) coated glasses were used as substrates. The FTO glasses were washed with acetone followed by deionized water under ultrasonic treatment for 1 h. Prior to use, the FTO glasses were sintered at 450 °C for 30 min. The electrode films were prepared by a doctor blade method using Scotch tape as the spacer. After dried in air, the films were sintered at 450 °C for 30 min. When room temperature was attained, the FTO glasses with thin films were cut into approximately 1.0 cm × 3.0 cm pieces with a film surface area of 1.0 cm × 1.0 cm.

The PEC measurements were performed with a three-electrode configuration system using Ag/AgCl as a reference electrode, the sample film as a working electrode, and Pt foil as a counter electrode. All the experiments were carried out in 0.5 M L^{-1} aqueous solution of Na$_2$SO$_4$. A set potential range from −0.4 V to 1.5 V vs Ag/AgCl was applied. As for PEC I-t curves measurement, the applied potential was 0.3 V vs Ag/AgCl electrode. The electrode films were irradiated with a 150 W Xe-lamp (Beijing, China), and the applied potential was controlled with a commercial computer controlled potentiostat (AUTOLAB PG STAT 101). Photocurrent action spectra as a function of visible-light excitation wavelength (λ ≤ 740 nm) were measured at 0.3 V bias vs Ag/AgCl.

2.4. Evaluation of the produced OH amount

For the measurement of OH amount, 0.05 g of each sample was taken and dispersed in 40 mL of 0.001 M coumarin aqueous solution contained in a quartz reactor. Prior to irradiation, the mixture was magnetically stirred for 30 min in dark to attain the adsorption-desorption equilibrium. After visible-light irradiation for 1 h, the mixture was centrifuged and a certain amount was transferred into a Pyrex glass cell for the fluorescence measurement of 7-hydroxycoumarin at 390 nm excitation wavelength and emission wavelength at 460 nm through a spectrofluorometer (Perkin-Elmer LS 55).

2.5. Evaluation of photocatalytic activities

The photocatalytic experiments for 2,4-DCP degradation were carried out in a 100 mL open photochemical glass reactor. For each experiment, 0.2 g of the sample was dispersed into 80 mL of (10 mg L^{-1}) 2,4-DCP solution. The solution was stirred for 30 min in dark, in order to reach the adsorption equilibrium. Then, the solution was irradiated under visible-light from a 150 W GYZ220 high-pressure Xenon lamp (Beijing, China) through a 420 nm cutoff filter. The samples were continuously stirred throughout the photocatalytic process. After regular interval of 30 min, a proper amount of the solution was centrifuged and the concentration of 2,4-DCP was analyzed by means of the characteristic optical absorption at 285 nm with a Model Shimadzu UV2550 spectrophotometer. The stability of the photocatalysts for photocatalytic degradation of 2,4-DCP was investigated by 4-times photocatalytic cycles. After each photocatalytic cycle for 3 h duration, the solution was extracted to measure the concentration of 2,4-DCP, whereas the used photocatalysts were collected and dried for the next cycle.

The intermediate products formed during the photocatalytic degradation of 2,4-DCP were analyzed with an Agilent liquid chromatography tandem mass spectrometry (1200/6410A, USA) technique. The fragments of the main intermediates were examined through scan mode. To measure the chloride ion concentration, a ThermorDionex ICS-600 ion chromatography equipped with an isocratic pump and a dialysis system was used. A mixture of aqueous solution of Na$_2$CO$_3$ (4.5 mmol L^{-1}) and NaHCO$_3$ (8.0 mmol L^{-1}) was used as the mobile phase. The flow rate of eluent was fixed at 0.8 mL min^{-1}. A 100 μL PEEK loop was used for samples injection. Duplicate runs were carried out on chromotography columns (Ion Pac AS23 4.0 × 250 mm). An AERS 500 eluent suppressor in an auto-recycle mode was used before the detector. The Chromeleon V6.8 chromatography data software was
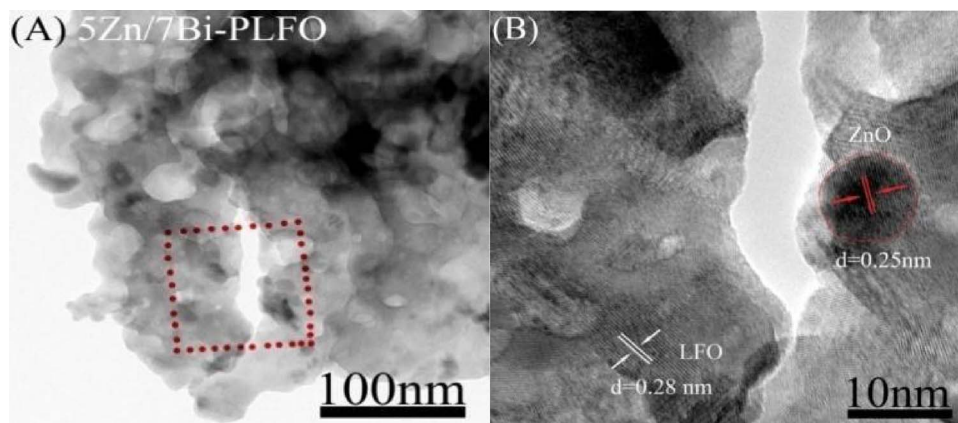
Fig. 1. TEM image (A) and HRTEM image (B) of 5Zn/7Bi-PLFO sample. PLFO means porous LaFeO₃, and X and Y in YZn/XBi-PLFO are the mole ratio percentages of used Bi and Zn to PLFO, respectively.

used to analyze and obtain the data. The standard stock solution (1000 µg mL^{-1}) of chlorine anions was purchased from Central Iron and Steel Research Institute. Standard solutions of chloride anions were prepared.

For photocatalytic experiments of CO_2 reduction, 0.2 g of each sample was dispersed in 3 ml water contained in a 100 ml volume cylindrical steel reactor with area 3.5 cm [2]. Then, high purity CO_2 gas was passed through the water and entered into the reaction setup to reach the ambient pressure. The CO_2/H_2O system containing the photocatalyst was allowed for 1 h to reach the equilibrium position. After that, the sample was irradiated with visible-light from a 300 W Xenon arc lamp (made in China) by a cutoff filter of 420 nm. During the irradiation period, about 0.5 ml of the gas was taken from the reaction cell at a given interval of time for the analysis of CO, CH_4 and O_2 concentrations. The concentration of CH_4 was detected with FID detector (GC-2014; with N_2 gas carrier, Shimadzu Corp., Japan), while the concentrations of CO and O_2 were detected with the help of a gas chromatograph (Tech, GC-7900 with TCD, N_2 gas carrier).

3. Results and discussion

3.1. Structural morphology and chemical composition

In order to investigate the crystal phase and crystallinity of the samples, XRD analysis was performed. The XRD patterns of PLFO, XBi-PLFO, YZn-PLFO and YZn/7Bi-PLFO samples respectively, are shown in Fig. S1A–C (ESI†). It is clear that PLFO exhibits intense diffraction peaks, which are the characteristic of highly crystalline product. These diffraction peaks are well-indexed to the orthorhombic phase with space group of Pbnm according to the JCPDS file No. 37-1493 [3]. No impurity peaks are observed, indicating the high quality product. For XBi-PLFO samples, the crystallographic phase of PLFO is not altered, even to the 10% doping level. From the enlarged views of main peaks (inset Fig. S1A, ESI†), it is clear that the diffraction peaks become wide and slightly shifted toward the lower diffraction angles, suggesting that the larger ionic radius Bi^{3+} cations (1.24 Å) are successfully incorporated into the crystal lattice of PLFO and partially substituted La^{3+} cations (1.22 Å). This is in accordance with the previous reports about Bi-doped perovskites [42,43]. The diffraction patterns of YZn-PLFO samples (Fig. S1B, ESI†) reveals that the introduction of ZnO does not change the crystal phase and crystallinity of PLFO. Interestingly, one can notice that the (1 0 1) diffraction peak of hexagonal ZnO appeared in the YZn-PLFO samples. However, the intensity of the peak is relatively low due to its small content. This is in good agreement with the previous report [44,45]. In addition, similar results are obtained for YZn/7Bi-PLFO samples as shown in Fig. S1C (ESI†). Therefore, it is deduced that Bi^{3+} entered into the crystal lattice of LFO while ZnO is

coupled onto the surfaces.

To investigate the optical absorption behavior of the samples, UV–vis DRS spectra were recorded. The DRS spectra of XBi-PLFO, YZn-PLFO and YZn/7Bi-PLFO samples are shown in Fig. S2A, B and C (ESI†). It can be seen from Fig. S2A (ESI†), that PLFO exhibits the absorption feature of a typical semiconductor originated by the electron transition from its valence band occupied by O2p orbital to the conduction band occupied by Fe3d orbital. Compared to PLFO, the reflection band edges of XBi-PLFO samples are obviously shifted toward longer wavelength direction with the increase in Bi content. This is attributed to the newly formed surface states related to Bi near the valence band top of PLFO. From the diffuse reflection band edges, the bandgaps of PLFO and 7Bi-PLFO samples are calculated to be about 2.0 eV and 1.77 eV respectively, according to the widely accepted energy bandgap equation $E_g = 1240/\lambda$. [3]. Hence, it is clear that the bandgap of XBi-PLFO samples is significantly reduced and exhibits an obvious absorption as compared to the PLFO. The DRS spectra of YZn-PLFO samples (Fig. S2B, ESI†) reveal that the introduction of ZnO does not affect the bandgap of PLFO. This indicates that ZnO is modified onto the surfaces of PLFO. As expected, similar DRS spectra are obtained for YZn/7Bi-PLFO samples, as shown in Fig. S2C (ESI†).

The morphology of as-prepared samples was investigated by means of TEM analysis. The TEM image of PLFO sample (Fig. S3A, ESI†) reveals that the sample exhibit porous structure. From HRTEM image (Fig. S3B, ESI†), it is clear that the pores exhibit average diameters in the range of 10–15 nm. The TEM image of 7Bi-PLFO sample (Fig. S3C, ESI†) reveals that the morphology of PLFO is not altered after doping Bi, and its HRTEM image (Fig. S3D, ESI†) shows the average pore diameters in the range of 10–15 nm. The TEM image of 5Zn-PLFO sample is shown in Fig. S3E (ESI†). While HRTEM image of 5Zn-PLFO sample is given in Fig. S3F (ESI†). It is obvious that the lattice fringes with d-spacing 0.28 nm corresponds to PLFO, while the later with d-spacing 0.25 nm is attributed to nanocrystalline ZnO [46,47]. The TEM image of 5Zn/7Bi-PLFO sample is shown in Fig. 1A, while the selected area HRTEM image of 5Zn/7Bi-PLFO sample is shown in Fig. 1B. From HRTEM image, it is noticed that an interface junction exists between 7Bi-PLFO and ZnO, since the lattice fringes with d-spacing of 0.25 nm are attributed to ZnO, while the lattice fringes with d-spacing of 0.28 nm correspond to PLFO.

The specific surface areas of PLFO, 7Bi-PLFO, 5Zn-PLFO and 5Zn/7Bi-PLFO samples were investigated by nitrogen adsorption-desorption isotherm measurements as shown in Fig. S4 (ESI†). From BET results (Fig. S4A, ESI†), it is confirmed that all the samples exhibit type IV isotherm curves, suggesting the existence of interconnected mesoporosity and high pore connectivity in the framework. It is noticed that PLFO exhibits a specific surface area of about 30.4 m^2 g^{-1}, while the observed surface areas for 7Bi-PLFO, 5Z-PLFO and 5Zn/7Bi-PLFO

samples are 32.3, 33.2 and 33.5 $m^2 g^{-1}$, respectively. Naturally expected, the large specific surface area is much beneficial for the better adsorption of substrates and provide more active sites for photocatalytic reactions. Further, the pore size distribution BJH method (Fig. S4B, ESI†) demonstrates that the average pore diameters of the samples lie in the range of 10–15 nm. The chemical composition of 7Bi-PLFO, 5Zn/PLFO and 5Zn/7Bi-PLFO samples was examined by energy-dispersive X-ray spectroscopy (EDX). The EDX spectrum of 7Bi-PLFO sample (Fig. S5A, ESI†) reveals the presence of Bi, La, Fe and O elements, and the EDX spectrum of 5Zn-PLFO sample (Fig. S5B, ESI†) reveals the presence of Zn, La, Fe and O elements. Similarly, the Zn, Bi, La, Fe and O elements exist in 5Zn/7Bi-PLFO sample according to the Fig. S5C (ESI†).

To further confirm the chemical compositions of PLFO, 7Bi-PLFO, 5Zn-PLFO and 5Zn/7Bi-PLFO samples, XPS analysis was performed as shown in Fig. S6 (ESI†). The typical survey spectra of PLFO, 7Bi-PLFO, 5Zn-PLFO and 5Zn/7Bi-PLFO samples are given in Fig. S6A (ESI†). One can see from the high-resolution XPS spectrum of La3d (Fig. S6B, ESI†), that there exist two main peaks located at 833.6 and 850.5 eV. The former is attributed to La $3d_{5/2}$, while the latter is ascribed to La $3d_{3/2}$ energy levels. It is clear that each peak presents a satellite at 4.0 eV higher, which is commonly attributed to the formation of hydroxyl on the surface and the spin-orbit splitting of La $3d_{5/2}$ and La $3d_{3/2}$ levels is 16.9 eV, indicating that La exists in +3 oxidation state [48]. The binding energies of Fe2p (Fig. S6C, ESI†), respectively at 710 ($2p_{3/2}$) and 723.6 eV ($2p_{1/2}$), correspond to the +3 oxidation state of Fe [49]. The XPS spectrum of O1s (Fig. S6D, ESI†) shows two distinct peaks at binding energies of 529.5 eV and 531.5 eV, respectively originated from the lattice oxide ions (OL) and the chemisorbed oxygen (OH) [3]. The XPS spectrum of Bi4f (Fig. S6E, ESI†) exhibits two strong peaks at binding energies of 163.8 eV and 158.5 eV, respectively, which correspond to the Bi $4f_{5/2}$ and Bi $4f_{7/2}$ energy levels [50]. It is obvious that the XPS peaks of La3d and Fe2p keep unchanged after doping Bi, while that of O1s slightly shifts toward the higher energy side. This indicates that Bi^{3+} is successfully incorporated into LFO, since the lattice oxygen peak of $BiFeO_3$ is located at binding energy of ~530 eV, a little higher than that of LFO [51,52]. The binding energies of Zn 2p for 5Zn/PLFO and 5Zn/7Bi- PLFO samples (Fig. S6F, ESI†), located at 1021 and 1044 eV, respectively, resulted from the Zn $2p_{3/2}$ and Zn $2p_{1/2}$ energy levels. Further, the spin-orbit splitting of Zn $2p_{3/2}$ and Zn $2p_{1/2}$ level is 23.0 eV, confirming that Zn mainly exists in +2 oxidation state [53]. In addition, it is seen that the XPS peaks of La3d, Fe2p, and O1s in the nanocomposites are slightly shifted toward lower energy side due to the coupled ZnO [32,46].

3.2. Photophysical and photochemical properties

The surface photovoltage (SPV) technique is a highly sensitive and non-destructive method used to investigate the photophysics of photogenerated charges in semiconducting solid materials. It is involved with steady-state surface photovoltage (SS-SPS) and time-resolved surface photovoltage (TR-SPV) responses. The SPV responses for nanocrystalline semiconductors mainly derive from photogenerated charge separation via the diffusion process [31]. In general, the strong SPV response always exhibit high photogenerated charge separation. The SS-SPS responses of PLFO, 7Bi-PLFO, 5Zn-PLFO and 5Zn/7Bi-PLFO samples in air atmosphere are shown in Fig. 2A, while those of XBi-PLFO, YZn-PLFO and YZn/7Bi-PLFO samples respectively, are given in Fig. S7A, B and C (ESI†). As shown in Fig. S7A (ESI†), PLFO exhibits weak SS-SPS response. However, it is greatly enhanced after doping Bi, and a remarkable increase is observed for 7Bi-PLFO, suggesting that the charge separation is obviously improved. Similarly, the SS-SPS responses of YZn-PLFO samples (Fig. S7B, ESI†) are remarkably high and much obvious for 5Zn-PLFO sample. Interestingly, the SS-SPS response of 7Bi-PLFO sample could be further enhanced after coupling with a proper amount of ZnO, especially for the amount-optimized 5Zn/7Bi-

PLFO sample (Fig. S7C, ESI†). However, if the amounts of used Bi and ZnO are in excess, the SS-SPS responses begin to decrease. From Fig. 2A, it is noticed that the SS-SPS response intensities are as follows: PLFO < 5Zn-PLFO < 7Bi-PLFO < 5Zn/7Bi-PLFO. This well demonstrates that the photogenerated charge separation of PLFO could be greatly enhanced after doping a proper amount of Bi and then coupling ZnO.

To further investigate the dynamic properties of photogenerated charge carriers, TR-SPV responses of PLFO and the amount-optimized 7Bi-PLFO, 5Zn-PLFO and 5Zn/7Bi-PLFO samples were measured under a laser pulse irradiation with 532 nm wavelength as shown in Fig. 2B. In general, the TR-SPV response of a semiconductor mainly involves two time ranges: the fast one ($< 10^{-5}$ s) arises from the charge separation by the built-in electric field and the slow one ($> 10^{-4}$ s) arises from the charge diffusion process. In general, it is positive in air since the photogenerated electrons are captured by the adsorbed O_2, while the holes could diffuse preferentially to the electrode surfaces. However, the fast-time signal of a nanosized semiconductor is usually very weak because of its neglectable built-in electric field. Thus, only the slow-time TR-SPV response could be observed [31]. It is clear that PLFO exhibits a weak TR-SPV signal in air. However, it is remarkably enhanced for 7Bi-PLFO and 5Zn-PLFO samples. In particular, the significant enhancement is observed for 5Zn/7Bi-PLFO sample with the prolonged lifetime of photogenerated charge carriers. This further supports the above SS-SPS results. As expected, one can see from Fig. 2C that PLFO exhibit a weak photocurrent density response. However, it is obviously enhanced for 7Bi-PLFO and 5Zn-PLFO samples, and the highest photocurrent response is detected for 5Zn/7Bi-PLFO sample. To further reveal the enhanced charge separation of the samples in photochemistry, the coumarin fluorescent method was used to detect the amount of produced OH radicals, in which the used coumarin reacts with OH radicals to produce 7-hydroxy coumarin. Thus, the intensity of fluorescence peak at approximately 453 nm can reflect the amount of produced OH radicals.

It is widely accepted that the OH radical is one of the most reactive species taking part in a variety of reaction pathways with inorganic and organic molecules [54]. The fluorescence spectra related to produced OH radicals of PLFO, 7Bi-PLFO, 5Zn-PLFO and 5Zn/7Bi-PLFO samples are shown in Fig. 2D, while those of XBi-PLFO, YZn-PLFO and YZn/7Bi-PLFO samples are given in Fig. S8A, B and C (ESI†). From Fig. S8A (ESI†), it is clear that PLFO produces a small amount of OH. However, its amount is greatly increased after doping Bi, especially for the amount-optimized 7Bi-PLFO sample. Similarly, the amount of OH produced by PLFO is greatly increased after coupling with ZnO (Fig. S8B, ESI†), and it is the largest for 5Zn-PLFO sample. Moreover, the amount of produced OH on 7Bi-PLFO could be further increased by coupling with ZnO (Fig. S8C, ESI†). In particular, 5Zn/7Bi-PLFO produces the largest amount of OH. Noticeably, the amount orders of the produced OH are in accordance with the above SPV and I–V results. This is also proved by the transient photocurrent results (I-t curves) with several on-off cycles of visible-light irradiation as shown in Fig. S8D (ESI†). Based on the above photophysical and photochemical measurements, it is concluded that the photogenerated charge separation of PLFO could be obviously enhanced by doping Bi and then coupling a proper amount ZnO.

3.3. Visible-light activities

The visible-light activities of the samples were evaluated for 2,4-DCP degradation. The photodegradation activities of PLFO, 7Bi-PLFO, 5Zn-PLFO and 5Zn/7Bi-PLFO samples are shown in Fig. 3A, while those of XBi-PLFO, YZn-PLFO and YZn/7Bi-PLFO samples are given in Fig. S9A–C (ESI†). For comparison, we have prepared the sample (MM-5Zn/7Bi-PLFO) by mechanically mixing ZnO and 7Bi-PLFO and evaluated its visible-light activity for 2,4-DCP degradation as shown in Fig. 3A. From Fig. S9A (ESI†), it is clear that PLFO exhibits weak photocatalytic
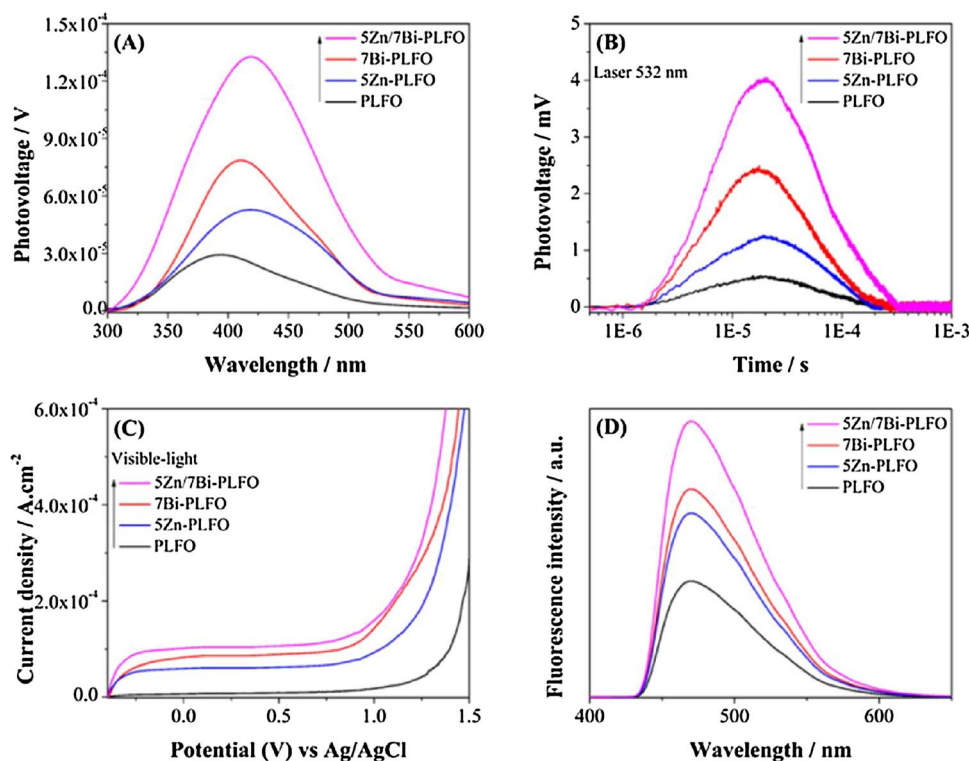
Fig. 2. SS-SPS spectra (A), TR-SPV responses (B), PEC I–V curves (C) and Fluorescence spectra related to hydroxyl radical amounts (D) of PLFO, 7Bi-PLFO, 5Zn-PLFO and 5Zn/7Bi-PLFO samples.

activity (28%) for 2,4-DCP degradation. However, its activity is greatly enhanced after doping Bi, and the highest activity (61%) is observed for 7Bi-PLFO sample. Similarly, the photocatalytic activities of YZn-PLFO samples (Fig. S9B, ESI†) for 2,4-DCP degradation are high, especially for the 5Zn-PLFO sample (i.e. 48%). Interestingly, as shown in Fig. S9C (ESI†), the photocatalytic activity of the amount-optimized 7Bi-PLFO sample is significantly improved after coupling with ZnO, and the highest photoactivity (77%) is observed for 5Zn/7Bi-PLFO sample. In comparison, the degradation rate of the MM-5Zn/7Bi-PLFO sample is 65%, which is a little higher than those of the PLFO, 7Bi-PLFO and 5Zn-PLFO samples. Hence, the nanocomposite formation of ZnO and Bi-PLFO is much beneficial for the improved photocatalytic activity. Further, if the amount of doped Bi and coupled ZnO are in excess, then it is unfavorable for the improved photocatalytic activity of PLFO. For practical applications, it is necessary to investigate the long-term stability of used photocatalysts during the photocatalytic processes. To study the reusability tests of 7Bi-PLFO, 5Zn-PLFO and 5Zn/7Bi-PLFO photocatalysts, photocatalytic recycle experiments were performed

under visible-light irradiation by adding the used photocatalysts to the fresh 2,4-DCP solutions. The amount of photocatalyst and 2,4-DCP concentration was constant. Noticeably, the photocatalytic activity of 7Bi-PLFO sample (Fig. S10A, ESI†), 5Zn-PLFO sample (Fig. S10B, ESI†) and 5Zn/7Bi-PLFO sample (Fig. S10C, ESI†) nearly retain unchanged after four successive photocatalytic recycles (each of 3 h), even unchanged after more than 10 times, under the same experimental conditions. This indicates that the fabricated PLFO-based photocatalysts are highly stable (especially the 5Zn/7Bi-PLFO one) during the photocatalytic degradation of 2,4-DCP.

To further confirm the enhanced visible-light activities for 2,4-DCP degradation, we have evaluated the visible-light activities of the samples for CO_2 conversion and O_2 production in water system in the absence of co-catalyst. The photocatalytic CO_2 reduction activities of PLFO, 7Bi-PLFO, 5Zn-PLFO, 5Zn/7Bi-PLFO samples are shown in Fig. 3B, while those of XBi-PLFO, YZn-PLFO and YZn/7Bi-PLFO are given in Fig. S11A–C (ESI†). For comparison, we have also measured the CO_2 reduction activity of the MM-5Zn/7Bi-PLFO sample as shown
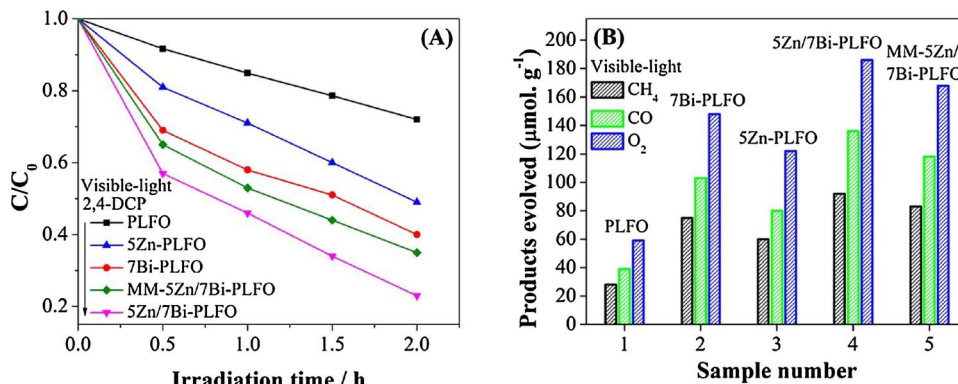

Fig. 3. Photocatalytic degradation rates of 2,4-DCP (A) and detected amounts of gas products in the CO_2 conversion (B) over PLFO, 7Bi-PLFO, 5Zn-PLFO, 5Zn/7Bi-PLFO and MM-5Zn/7Bi-PLFO samples.

in Fig. 3B. It is confirmed that the detected gases contain CH_4 and CO as the reduction products, while O_2 as the oxidation product. From Fig. S11A (ESI†), it is obvious that PLFO exhibit weak photocatalytic activities for CO_2 conversion to CH_4 ($\sim$28 μmol) and CO ($\sim$39 μmol), and for producing O_2 ($\sim$59 μmol) under visible-light irradiation for 6 h. However, its photoactivities are greatly enhanced after doping Bi, especially for the amount optimized 7Bi-PLFO sample that produced CH_4 ($\sim$75 μmol), CO ($\sim$103 μmol) and O_2 ($\sim$148 μmol). As expected, the visible-light activities of PLFO sample (Fig. S11B, ESI†) for CO_2 conversion and O_2 production are greatly improved after coupling with ZnO, and the amount-optimized 5Zn-PLFO sample produced CH_4 ($\sim$60 μmol) CO ($\sim$80 μmol) and O_2 ($\sim$122 μmol). Interestingly, as shown in Fig. S11C (ESI†), the photocatalytic activities of the amount optimized 7Bi-PLFO sample for CO_2 conversion and O_2 production are significantly improved after coupling with ZnO, and the largest amounts of CH_4 ($\sim$92 μmol), CO ($\sim$136 μmol) and O_2 ($\sim$186 μmol) are detected for 5Zn/7Bi-PLFO sample. Notably, the MM-5Zn/7Bi-PLFO sample produces CH_4 ($\sim$83 μmol), CO ($\sim$118 μmol) and O_2 ($\sim$168 μmol), which is also a little higher than those of the PLFO, 7Bi-PLFO and 5Zn-PLFO samples. This reveals that coupling ZnO is much favorable for charge transfer and separation and the improved photocatalytic activities of LFO. The amounts of product detected in our experiments are much higher than those in the previous works [3,55]. Naturally deduced, the significantly improved visible-light activities of PLFO for 2,4-DCP degradation and CO_2 conversion are attributed to the enhanced charge separation by doping Bi^{3+} and coupling with ZnO.

3.4. Charge transfer mechanism

To confirm the extended visible-light absorption, the valence band XPS spectra of PLFO, 7Bi-PLFO and 5Zn/7Bi-PLFO samples were measured as shown in Fig. 4A. It is clear that the VB positions of 7Bi-PLFO and 5Zn/7Bi-PLFO samples are shifted to 1.97 eV in comparison to that of PLFO (2.2 eV). This is attributed to the Bi introduced surface states near the VB top of PLFO. Hence, it is confirmed that the bandgap of PLFO is effectively reduced after doping Bi^{3+}. From the valence band XPS spectra, the bandgaps of 7Bi-PLFO and 5Zn/7Bi-PLFO samples are calculated to be 1.77 eV, which is in accordance with the DRS results. The photocurrent action spectra as a function of visible-light excitation wavelengths ($\lambda \leq 740$ nm) measured at 0.3 V bias vs Ag/AgCl in 0.5 M L^{-1} Na_2SO_4 electrolyte solution are shown in Fig. 4B. One can see that PLFO exhibits a weak photocurrent response at wavelength 620 nm, which is closely associated to the bandgap of 2.0 eV, and the photocurrent response is remarkably enhanced with the decrease in the excitation wavelengths. As for 7Bi-PLFO sample, an obvious photocurrent response is observed at 700 nm, which is in accordance with the energy bandgap of 1.77 eV, and the photocurrent response is gradually

enhanced with the decrease in excitation wavelengths. Noticeably, the photocurrent response of Bi-doped PLFO is higher than that of PLFO at the same excitation wavelengths. This is because that the introduced surface states are favorable for the enhanced charge separation based on the above SPV results. Further, it is noticed that an obviously enhanced photocurrent response begins at 540 nm for 5Zn/PLFO sample, while it begins at 600 nm for 5Zn/7Bi-PLFO one. As expected, the photocurrent response is continuously enhanced with the decrease in excitation wavelengths. This obviously enhanced photocurrent response is attributed to the transfers of visible-light excited high-level-energy electrons (HLEEs) to ZnO. To well understand the enhanced charge separation mechanism for the fabricated 5Zn/7Bi-PLFO nanocomposite, a schematic is designed as shown in Fig. 5. According to the previous report [33], the bandgap of ZnO is 3.2 eV, and its VB top and CB bottom are respectively located at 3.1 eV and -0.1 eV, versus SHE. Hence, ZnO can be excited by the photon energy with wavelengths ($\lambda \leq 387$ nm). On the other hand, PLFO exhibits a bandgap of approximately 2.0 eV, corresponding to the light absorption threshold at 620 nm. Further, it is demonstrated that the VB top and CB bottom of PLFO are located at 2.2 eV and 0.2 eV respectively, versus NHE. Thus, the energy difference between the VB top of PLFO and the CB bottom of ZnO is $\sim$2.3 eV, corresponding to the light energy of approximately $\lambda = 540$ nm, based on the widely-accepted energy bandgap equation ($\lambda = 1240/E_g$). Hence, the excited HLEEs of PLFO with the visible-light below 540 nm would transfer thermodynamically to ZnO so as to promote the charge separation. Similarly, it is evaluated that the energy difference between the VB top of 7Bi-PLFO and the CB bottom of ZnO is $\sim$2.07 eV, related to the light energy of wavelength 600 nm. Thus, it is acceptable that the threshold wavelength for producing HLEEs to transfer thermodynamically to ZnO is modulated from 540 nm on PLFO to 600 nm on Bi-doped PLFO, and it is the effective visible-light range for HLEEs from the threshold wavelength to 400 nm.

Therefore, it is deduced that the utilization of visible-light excited HLEEs could be greatly improved by doping Bi^{3+} to extend the visible-light absorption and coupling ZnO to accept HLEEs, leading to the greatly-enhanced photocatalytic activities for 2,4-DCP degradation and CO_2 conversion. Naturally expected, the HLEEs transferred to ZnO should possess enough energy to induce the reduction reactions with O_2 to produce $O_2^{\cdot-}$ in the degradation of 2,4-DCP, and with H_2O or CO_2 in the process of CO_2 conversion. This greatly solves the low CB bottom shortcoming. Besides, the produced holes at the VB top and at the surface states could possess enough energy to initiate the oxidation reactions with H_2O to produce OH. These highly reactive species would further participate in the photocatalytic reactions. Hence, it is of great significance to utilize the photogenerated HLEEs of perovskite-type oxides to make the visible-light activities more practical for environmental remediation and energy production.
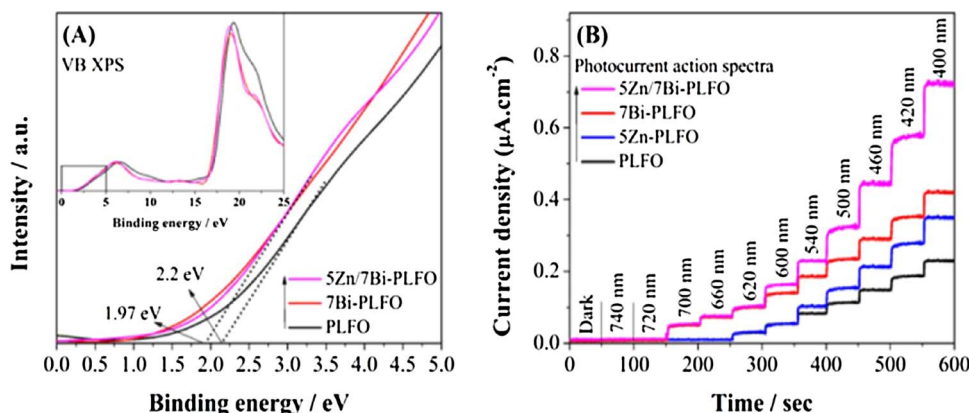

Fig. 4. Valence band XPS spectra (A) of PLFO, 7Bi-PLFO and 5Zn/7Bi-PLFO samples and photocurrent action spectra as a function of visible-light excitation wavelengths ($\lambda \leq 740$ nm) at 0.3 V bias vs Ag/AgCl in 0.5 M L^{-1} Na_2SO_4 (B) of PLFO, 7Bi-PLFO, 5Zn-PLFO and 5Zn/7Bi-PLFO samples.
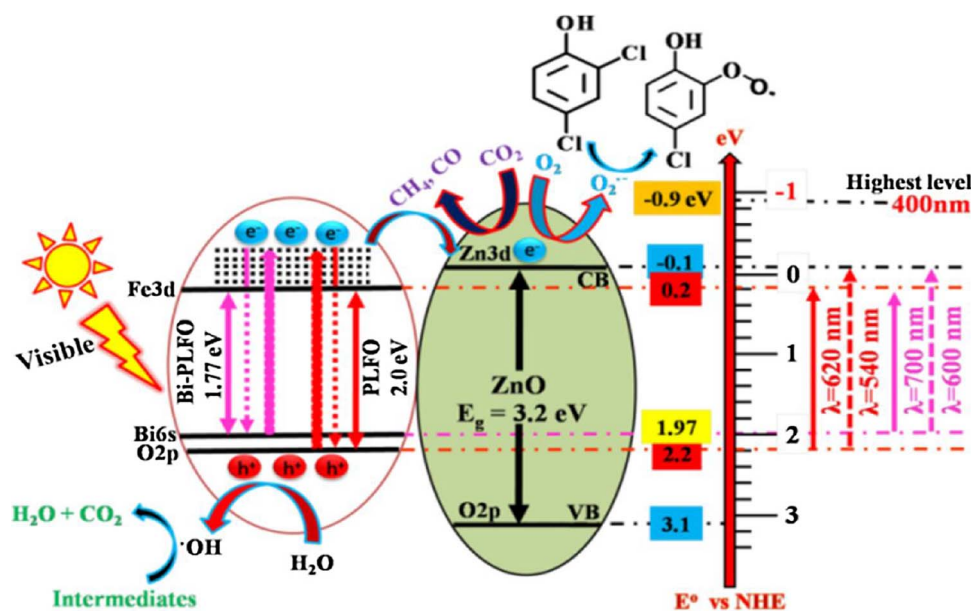
Fig. 5. Schematic of the energy bandgap structures, the charge transfer and separation in 5Zn/7Bi-PLFO nanocomposite under visible-light irradiation.

3.5. 2,4-DCP degradation paths

It is widely accepted that the photocatalytic degradation of organic compounds proceeds via three routes: direct oxidation by the positively charged holes (h^+), oxidation by OH and superoxide radicals ($O_2^{\cdot-}$). To make sure about the main active species taking part in the photocatalytic degradation of 2,4-DCP, Isopropyl alcohol (IPA), Benzoquinone (BQ) and EDTA-2Na as scavenging species were used to investigate the roles of OH, $O_2^{\cdot-}$ and h^+, respectively [56–59]. A desired amount of the scavengers (1 mM) was added to 80 mL of the 2,4-DCP solution prior to the catalyst addition and vigorously stirred for 10 min. From Fig. S12A (ESI†), one can see that the degradation of 2,4-DCP over PLFO is slightly suppressed in the presence of BQ and IPA scavengers, while it is strongly inhibited in the presence of EDTA-2Na. This means that the photogenerated holes is the main oxidant to dominantly induce the photocatalytic degradation of 2,4-DCP over PLFO. As shown in Fig. S12B (ESI†), the degradation of 2,4-DCP over 5Zn/PLFO photocatalyst is slightly suppressed in the presence of IPA and EDTA-2Na, while it is strongly inhibited in the presence of BQ, suggesting that the $O_2^{\cdot-}$ is dominant for the photocatalytic degradation of 2,4-DCP over 5Zn/PLFO sample. One can see from Fig. 6A, that the degradation of 2,4-DCP over 7Bi-PLFO photocatalyst is slightly suppressed in the presence of BQ and EDTA-2Na, while it is strongly inhibited in the presence of IPA. Hence, it is confirmed that the OH is

the predominant active intermediate contributing to the degradation of 2,4-DCP over 7Bi-PLFO photocatalyst, while the role of $O_2^{\cdot-}$ and h^+ is less significant. To further investigate the photocatalytic degradation of 2,4-DCP over 5Zn/7Bi-PLFO sample, same conditions were applied.

From Fig. 6B, it is obvious that the degradation of 2,4-DCP over 5Zn/7Bi-PLFO photocatalyst is slightly suppressed in the presence of IPA and EDTA-2Na, while it is strongly inhibited in the presence BQ. Hence, it is confirmed that the produced $O_2^{\cdot-}$ is the predominant active specie taking part in the degradation of 2,4-DCP over 5Zn/7Bi-PLFO. Further, the UV–vis-light activities of PLFO, 7Bi-PLFO, 5Zn-PLFO and 5Zn/7Bi-PLFO samples for 2,4-DCP degradation were measured and compared with that of the commercially available P25 TiO2. Fig. S13A (ESI†) clearly demonstrates that the UV–vis-light activities of the samples are remarkably improved compared to that of the visible-light activities. Interestingly, the UV–vis-light activity of 5Zn/7Bi-PLFO sample for 2,4-DCP is much significant as compared to that of P25 TiO2. Hence, it is confirmed that the 5Zn/7Bi-PLFO photocatalyst is highly efficient for degrading organic pollutants.

In addition, the scavenger trapping experiments were performed under UV–vis-light irradiation to investigate the degradation mechanism of 2,4-DCP over 5Zn/7Bi-PLFO and P25 samples. From Fig. S13B (ESI†), one can notice that the degradation of 2,4-DCP over 5Zn/7Bi-PLFO and P25 TiO2 photocatalysts is slightly suppressed in the presence of IPA and EDTA-2Na scavengers, while it is strongly inhibited
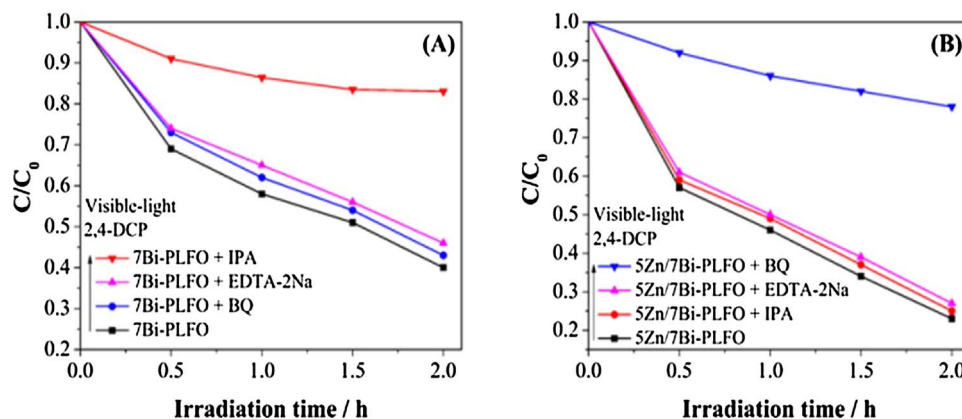

Fig. 6. Scavenger trapping experiments on 7Bi-PLFO (A) and 5Zn/7Bi-PLFO (B).

in the presence of BQ. Hence, it is confirmed that the produced $O_2^{\cdot-}$ is the dominant oxidant to initiate the photocatalytic degradation of 2,4-DCP over 5Zn/7Bi-PLFO and P25 TiO_2 samples.

In order to clarify the photocatalytic degradation mechanism of 2,4-DCP over 7Bi-PLFO photocatalyst, liquid chromatography tandem mass spectrometry analysis of the intermediates was carried out after visible-light irradiation for 2 h. The extract ion chromatography (EIC) signals of the intermediates were recorded with retention time between 0–15 min. It is obvious that the OH directly attacks the aromatic ring of 2,4-DCP and remove a single chloride to yield 4-chlorophenol ($m/z = 127.5$, Fig. S14A, ESI†) as the first key step [60]. In the second step, the OH further attacks the aromatic ring of 4-chlorophenol and produce 4-chlorobenzene-1,2-diol ($m/z = 143.5$, Fig. S14B, ESI†), as confirmed by the EIC signal with retention time of 3.2 min. This is further supported by the liquid chromatography tandem mass spectrometry product ion fragments of the main intermediate 4-chlorobenzene-1,2-diol ($m/z = 143.5$), as inset in Fig. S14B (ESI†). It is clear that the fragments such as benzoquinone ($m/z = 107$), perchlorate ($m/z = 98.5$), acetyl chloride ($m/z = 78.5$), formic acid ($m/z = 45$), cyclopropyl ($m/z = 41$) and chloride ($m/z = 35$) are the resultant decomposition products. In third step, the OH attacks the aromatic ring of 4-chlorobenzene-1,2-diol and yields two reversible products such as 5-chlorobenzene-1,2,4-triol ($m/z = 159.5$, Fig. S14C, ESI†) and 2-chloro-5-hydroxy-1,4-benzoquinone ($m/z = 157.5$, Fig. S14D, ESI†) as confirmed by the EIC signals. It is obvious that the fragments such as 2-hydroxy-1,4-benzoquinone ($m/z = 123$), chloroacetic acid ($m/z = 94.5$) and acetyl chloride ($m/z = 78.5$) are the resultant decomposition products of 5-chlorobenzene-1,2,4-triol. In fourth step, the OH attacks the aromatic ring of 5-chlorobenzene-1,2,4-triol and remove the second chloride to yield 2-hydroxy-1,4-benzoquinone ($m/z = 123$, Fig. S14E, ESI†), which further transform into phenol ($m/z = 93$, Fig. S14F, ESI†). At this stage, the aromatic ring ruptures and low molecular weight products like acetic acid ($m/z = 59$, Fig. S14G, ESI†) and formic acid ($m/z = 45$, Fig. S14H, ESI†) are produced, which readily transforms into inorganic minerals CO_2 and H_2O [39,61–65]. Based on the resultant intermediates, a schematic pathway for 2,4-DCP degradation over 7Bi-PLFO

photocatalyst is proposed as depicted in Scheme 1.

In order to support the above results, the chloride ion concentration was measured with ion chromatography technique after visible-light photocatalytic degradation of 2,4-DCP over 7Bi-PLFO sample for 2 h. The experimentally detected chloride concentration is $\sim 2.02\,mg\,L^{-1}$, which is in good agreement with the theoretical value $2.65\,mg\,L^{-1}$ for the fully removed chloride from the aromatic ring of 2,4-DCP. In addition, the EIC products were detected at different irradiation period i.e. 30, 60, 90 and 120 min, as shown in Fig. S15 (ESI†). It is obvious that the amounts of intermediates with m/z values 143.5, 159.5, 157.5 and 123 are apparently large at 90 min. However, the amounts are gradually decreased with the prolonged irradiation period i.e. 120 min. Hence, it is suggested that the degradation of 2,4-DCP by OH gradually increase with the increase in the irradiation period. Based on the key steps for Cl- removal, it is demonstrated that the OH should play a vital role in the degradation of 2,4-DCP. To investigate the degradation mechanism of 2,4-DCP over 5Zn/7Bi-PLFO photocatalyst after visible-light irradiation for 2 h, the resultant intermediate products were detected with the help of liquid chromatography tandem mass spectrometry technique as shown in Fig. S16 (ESI†). The extract ion chromatography (EIC) signals were recorded with a retention time of 0 to 10 min. It is clear that in the first step, $O_2^{\cdot-}$ directly attacks the aromatic ring of 2,4-DCP and produce parachlorophenol superoxide radical ($m/z = 159.5$, Fig. S16A, ESI†) by the removal of a single Cl^-. In the second step, OH attacks the aromatic ring of parachlorophenol superoxide radical and produce 4-chlorobenzene-1,2-diol ($m/z = 143.5$, Fig. S16B, ESI†). In third step, the $O_2^{\cdot-}$ attacks the aromatic ring of 4-chlorobenzene-1,2-diol and yield benzene-1,2-diol superoxide radical ($m/z = 141$, Fig. S16C, ESI†), by removing the second Cl^-. Further, the OH favors the attack of aromatic ring and produce 2-hydroxy-1,4-benzoquinone ($m/z = 123$, Fig. S16D, ESI†). This is further supported by the liquid chromatography tandem mass spectrometry product ion fragments of the main intermediate 2-hydroxy-1,4-benzoquinone ($m/z = 123$), as inset in Fig. S16D (ESI†). It is clear that the fragments phenol ($m/z = 93$), ethylene glycol ($m/z = 62$), and cyclopropyl ($m/z = 41$) are the resultant decomposition products. In fourth step, the
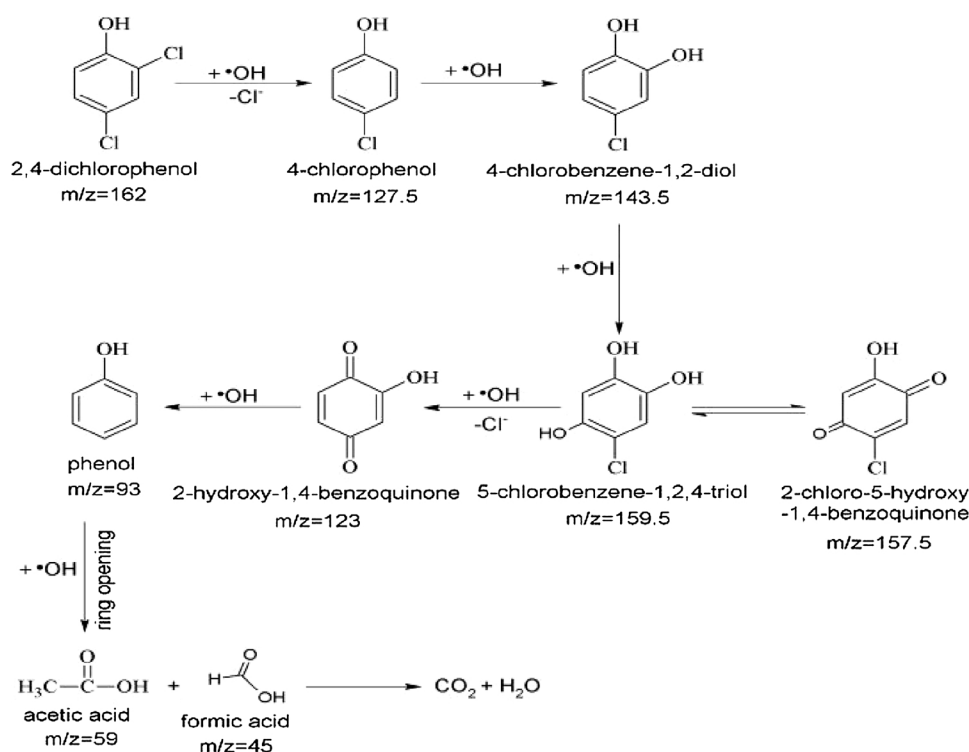
Scheme 1. Proposed pathway for the visible-light photocatalytic degradation of 2,4-DCP over 7Bi-PLFO photocatalyst.
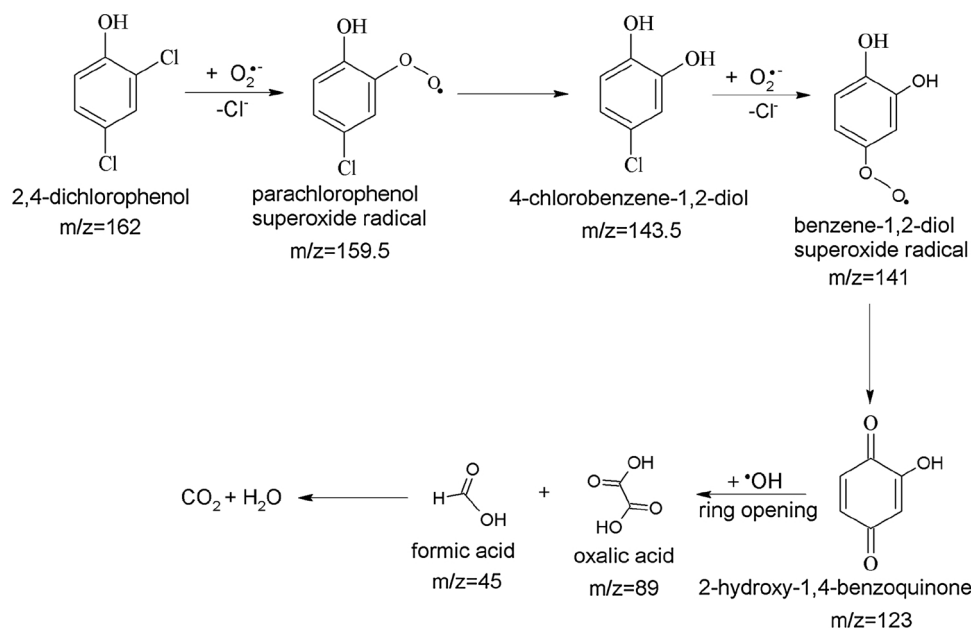
Scheme 2. Proposed pathway for the visible-light photocatalytic degradation of 2,4-DCP over 5Zn/7Bi-PLFO photocatalyst.

aromatic ring of 2-hydroxy-1,4-benzoquinone ruptures by the attack of OH and low molecular weight products such as oxalic acid ($m/z = 89$, Fig. S16E, ESI†) and formic acid ($m/z = 45$, Fig. S16F, ESI†) are produced, which then transforms into inorganic minerals CO_2 and H_2O [39,60–65]. Based on the resultant intermediates, a schematic pathway for 2,4-DCP degradation over 5Zn/7Bi-PLFO photocatalyst is proposed as shown in Scheme 2.

To further prove that the super oxide radical ($O_2^{\cdot-}$) is involved in the photocatalytic degradation of 2,4-DCP over 5Zn/7Bi-PLFO photocatalyst, the experiments were performed in pure D_2O. It is clear that after visible-light irradiation for 2h, the m/z values of the product ions 4-chlorobenzene-1,2-diol (Fig. S17A, ESI†), benzene-1,2-diol superoxide radical (Fig. S17B, ESI†) and 2-hydroxy-1,4-benzoquinone (Fig. S17C, ESI†) are increased by 1 due to the used D_2O. Hence, it is confirmed that the $O_2^{\cdot-}$ is the predominant oxidant involved in the degradation of 2,4-DCP over 5Zn/7Bi-PLFO photocatalyst. In order to support the above results, the chloride ion concentration was measured with ion chromatography technique after visible-light photocatalytic degradation of 2,4-DCP over 5Zn/7Bi-PLFO sample for 2 h. Obviously, the detected chloride concentration is $\sim 3.15\,\mathrm{mg\,L^{-1}}$, which is in good agreement with the theoretical value $3.35\,\mathrm{mg\,L^{-1}}$ for the fully removed chloride from the aromatic ring of 2,4-DCP. To investigate the effect of irradiation time on the produced intermediates, the EIC products at different irradiation periods i.e. 30, 60, 90 and 120 min were detected with the help of liquid chromatography tandem mass spectrometry technique as shown in Fig. S18 (ESI†). Noticeably, the amount of intermediate with m/z value of 143.5 is obviously decreased at 120 min compared to the amounts of intermediates with m/z values of 141, 123, 89 and 45 at the same irradiation period, suggesting that the subsequent degradation of 2,4-DCP by $O_2^{\cdot-}$ is a rather fast process. Based on the key steps for Cl^- removal, it is demonstrated that the $O_2^{\cdot-}$ could play a vital role in the degradation of 2,4-DCP.

4. Conclusions

We have successfully synthesized ZnO/Bi-doped PLFO nanocomposites via a wet-chemical method. It is shown that the amount-optimized 5Zn/7Bi-PLFO nanocomposite exhibits significantly improved visible-light activities for 2,4-DCP degradation and CO_2 conversion compared to the unmodified PLFO. Based on the experimental results, it is confirmed that the significantly improved visible-light activities are attributed to the enhanced utilization of visible-light-excited HLEEs by extending visible-light absorption via the Bi-introduced surface states and coupling ZnO to introduce a suitable high-level-energy platform for accepting electrons. Interestingly, it is confirmed that the UV–vis-light photocatalytic activities of the amount-optimized sample for 2,4-DCP degradation is much obvious compared to the P25 TiO$_2$. Moreover, it is confirmed that the produced highly reactive species could be modulated to dominantly decompose 2,4-DCP over PLFO by doping Bi and then coupling ZnO. Furthermore, the possible decomposition pathways of 2,4-DCP over the amount-optimized 7Bi-PLFO and 5Zn/7Bi-PLFO samples, respectively related to the OH and $O_2^{\cdot-}$, are proposed. This work opens up a new feasible strategy for the synthesis of highly-efficient visible-light-active perovskite-type nano-photocatalysts for environmental remediation and solar fuel production.

Appendix A. Supplementary data

Supplementary material related to this article can be found, in the online version, at doi:https://doi.org/10.1016/j.apcatb.2018.02.060.

References

[1] X.G. Duan, H.Q. Sun, J. Kang, Y.X. Wang, S. Indrawirawan, S.B. Wang, ACS Catal. 5 (2015) 4629.
[2] J. Xu, Z. Cao, X. Liu, H. Zhao, X. Xiao, J.P. Wu, X.H. Xu, J.L. Zhou, J. Hazard. Mater. 317 (2016) 656.
[3] M. Humayun, Y. Qu, F. Raziq, R. Yan, Z.J. Li, X.L. Zhang, L.Q. Jing, Environ. Sci. Technol. 50 (2016) 13600.
[4] H.P. Rong, S.F. Cai, Z.Q. Niu, Y.D. Li, ACS Catal. 3 (2013) 1560.
[5] J.H. Choi, Y.H. Kim, J. Hazard. Mater. 166 (2009) 984.
[6] Z. Bian, F. Cao, J. Zhu, H. Li, Environ. Sci. Technol. 49 (2015) 2418.

[7] K. Li, B. Peng, T.Y. Peng, ACS Catal. 6 (2016) 7485.
[8] C.R. Somnath, K.V. Oomman, P. Maggie, A.G. Craig, ACS Nano 3 (2010) 1259.
[9] J. Qiao, Y. Liu, F. Hong, J. Zhang, Chem. Soc. Rev. 43 (2014) 631.
[10] J.A. Modestra, B. Navaneeth, S.V. Mohan, J. CO2 Util. 10 (2015) 78.
[11] X.Y. Ji, Z.G. Su, M.F. Xu, G.H. Ma, S.P. Zhang, ACS Sustain. Chem. Eng. 4 (2016) 3634.
[12] Z.F. Bian, J. Zhu, H.X. Li, J. Photochem. Photobiol. C 28 (2016) 72.
[13] C. Tang, L.F. Liu, Y. Li, Z.F. Bian, Appl. Catal. B Environ. 201 (2017) 41.
[14] Y. Li, Y.Y. Bian, H.X. Qin, Y. Zhang, Z.F. Bian, Appl. Catal. B Environ. 206 (2017) 293.
[15] H.X. Qin, Y.Y. Bian, Y. Zhang, L.F. Liu, Z.F. Bian, Chin. J. Chem. 35 (2017) 203.
[16] R.C. Li, X.Y. Jin, M. Megharaj, R. Naidu, Z.L. Chen, Chem. Eng. J 264 (2015) 587.
[17] L.F. Liu, F. Chen, F.L. Yang, Y.S. Chen, J. Crittenden, Chem. Eng. J 181 (2012) 189.
[18] K.R. Ganganahalli, F.B. Joan, V.K. Prashant, ACS Catal. 4 (2014) 3249.
[19] L.J. Liu, Y.Q. Jiang, H.L. Zhao, J.T. Chen, J.L. Cheng, K.S. Yang, Y. Li, ACS Catal. 6 (2016) 1097.
[20] M.Z. Xie, J. Bian, M. Humayun, Y. Qu, Y.J. Feng, L.Q. Jing, Chem. Commun. 51 (2015) 2821.
[21] F. Teng, Z.L. Liu, A. Zhang, M. Li, Environ. Sci. Technol. 49 (2015) 9489.
[22] T. Soltani, B.K. Lee, Chem. Eng. J. 313 (2017) 1258.
[23] E.O. Scott-Emuakpor, A. Kruth, M.J. Todd, A. Raab, G.I. Paton, D.E. Macphee, Appl. Catal. B Environ. 123 (2012) 433.
[24] E.L. Yang, J.J. Shi, H.C. Liang, W.K. Cheuk, Chem. Eng. J. 174 (2011) 539.
[25] X.Y. Chen, Y. Zhou, Q. Liu, Z.D. Li, J.G. Liu, Z.G. Zou, ACS Appl. Mater. Interfaces 4 (2012) 3372.
[26] S. Gao, B.C. Gu, X.C. Jiao, Y.F. Sun, X.L. Zu, F. Yang, W.G. Zhu, C.M. Wang, Z. Feng, B.J. Ye, Y. Xie, J. Am. Chem. Soc. 139 (2017) 3438.
[27] C. Srilakshmi, R. Saraf, C. Shivakumara, Ind. Eng. Chem. Res. 54 (2015) 7800.
[28] L.Q. Jing, Y. Qu, H.J. Su, C.H. Yao, H.G. Fu, J. Phys. Chem. C 115 (2011) 12375.
[29] J.J. Xu, Z.L. Wang, D. Xu, F.Z. Meng, X.B. Zhang, Energy Environ. Sci. 7 (2014) 2213.
[30] P. Luan, M.Z. Xie, X.D. Fu, Y. Qu, X.J. Sun, L.Q. Jing, Phys. Chem. Chem. Phys. 17 (2015) 5043.
[31] M.Z. Xie, X.D. Fu, L.Q. Jing, P. Luan, Y.J. Feng, H.G. Fu, Adv. Energy Mater. 4 (2014) 1300995.
[32] M. Humayun, A. Zada, Z.J. Li, M.Z. Xie, X.L. Zhang, Y. Qu, F. Raziq, L.Q. Jing, Appl. Catal. B Environ. 180 (2016) 219.
[33] X. Guo, Z.H. Jun, L. Quan, Appl. Catal. B Environ. 160 (2014) 408.
[34] H. Wu, R. Hu, T. Zhou, C. Li, W. Meng, J. Yang, CrystEngComm 17 (2015) 3859.
[35] G. Iervolino, V. Vaiano, D. Sannino, L. Rizzo, V. Palma, Appl. Catal. B Environ. 207 (2017) 182.
[36] Y.B. Ding, F. Yang, L.H. Zhu, N. Wang, H.Q. Tang, Appl. Catal. B Environ. 164 (2015) 151.
[37] Y.X. Wang, H.Q. Sun, H.M. Ang, M.O. Tade, S.B. Wang, Appl. Catal. B Environ. 164

[38] L.K. Weavers, N. Malmstadt, M.R. Hoffmann, Environ. Sci. Technol. 34 (2000) 1280.
[39] H.Y. Zhou, Q. Sun, X. Wang, L.L. Wang, J. Chen, J.D. Zhang, X.H. Lu, Sep. Purif. Technol. 132 (2014) 346.
[40] T. Luo, Z.H. Ai, L.Z. Zhang, J. Phys. Chem. C 112 (2008) 8675.
[41] H.M. Jia, W.W. He, W.G. Wamer, X. Han, B.B. Zhang, S. Zhang, Z. Zheng, Y. Xiang, J.J. Yin, J. Phys. Chem. C 118 (2014) 21447.
[42] M. Li, Y. Wang, Y.L. Wang, F.L. Chen, C.G. Xia, ACS Appl. Mater. Interfaces 6 (2014) 11286.
[43] M.A. Ahmed, A.A. Azab, E.H.E. Khawas, J. Mater. Sci. 26 (2015) 8765.
[44] N. Zhang, F.Y. Cheng, Y.C. Liu, Q. Zhao, K.X. Lei, C.C. Chen, X.S. Liu, J. Chen, J. Am. Chem. Soc. 138 (2016) 12894.
[45] A. Hamrouni, N. Moussa, A.D. Paola, F. Parrino, A. Houas, L. Palmisano, Appl. Catal. B Environ. 154 (2014) 379.
[46] Q. Zhang, Y. Huang, S.Q. Peng, Y.F. Zhang, Z.X. Shen, J.J. Cao, W.K. Ho, S.C. Lee, D.Y.H. Pui, Appl. Catal. B Environ. 204 (2017) 346.
[47] B.M. Rajbongshi, S.K. Samdarshi, Appl. Catal. B Environ. 144 (2014) 435.
[48] J. Faye, A. Baylet, M. Trentesaux, S. Royer, F. Dumeignil, D. Duprez, S. Valange, J. Tatibouet, Appl. Catal. B Environ. 126 (2012) 134.
[49] D. Pasinski, E. Zych, J. Sokolnicki, J. Alloy. Compd. 668 (2016) 194.
[50] P.D. Kanhere, J.W. Zheng, Z. Chen, J. Phys. Chem. C 115 (2011) 11846.
[51] W.W. Meng, R.S. Hu, J. Yang, Y.F. Du, J.J. Li, H.Y. Wang, Chin. J. Catal. 37 (2016) 1283.
[52] K. Sutthiumporn, T. Maneerung, Y. Kathiraser, S. Kawi, Int. J. Hydrogen Energy 37 (2012) 11195.
[53] Y.W. Yang, W.X. Que, X.Y. Zhang, X.T. Yin, Y.L. Xing, M.D. Que, H.Y. Zhao, Y.P. Du, Appl. Catal. B Environ. 400 (2017) 402.
[54] S. Gligorovski, R. Strekowski, S. Barbati, D. Vione, Chem. Rev. 115 (2015) 13051.
[55] Q. Jiang, Z. Chen, J. Tong, M. Yang, Z. Jiang, C. Li, ACS Catal. 6 (2016) 1172.
[56] M. Rakibuddin, R. Ananthakrishnan, Photochem. Photobiol. Sci. 15 (2016) 86.
[57] J. Di, J.X. Xia, M.X. Ji, B. Wang, S. Yin, H. Xu, Z.G. Chen, Langmuir 32 (2016) 2075.
[58] S. Khanchandani, S. Kumar, A.K. Ganguli, ACS Sustain. Chem. Eng. 4 (2016) 1487.
[59] W. Teng, X.Y. Li, Q.D. Zhao, J.J. Zhao, D.K. Zhang, Appl. Catal. B Environ. 125 (2012) 538.
[60] Y. Liu, Y. Zhu, J. Xu, X. Bai, R. Zong, Y. Zhu, Appl. Catal. B Environ. 142 (2013) 561.
[61] H. Liu, X. Ruan, D.Y. Zhao, X.Y. Fan, T. Feng, Ind. Eng. Chem. Res. 56 (2017) 191.
[62] H.F. Wang, Y.S. Zhao, Y. Su, T.Y. Li, M. Yao, C.Y. Qin, RSC Adv. 7 (2017) 4563.
[63] X. Li, M.H. Zhou, Y.W. Pan, L. Xu, Chem. Eng. J 307 (2017) 1092.
[64] K. Su, Z.H. Ai, L.Z. Zhang, J. Phys. Chem. C 116 (2012) 17118.
[65] Y.J. Qian, J. Zhang, Y.L. Zhang, J.B. Chen, X.F. Zhou, Sep. Purif. Technol. 166 (2016) 222.